The Astrophysical Journal, 889:172 (10pp), 2020 February 1 https://doi.org/10.3847/1538-4357/ab5e79

Resolving Linear Polarization due to Emission and Extinction of Aligned Dust Grains on NGC 1333 IRAS4A with JVLA and ALMA

Chia-Lin Ko (柯嘉琳)[1,2], Hauyu Baobab Liu (呂浩宇)[2,3], Shih-Ping Lai (賴詩萍)[1], Tao-Chung Ching (慶道沖)[4,5], Ramprasad Rao[2], and Josep Miquel Girart[6,7]
[1] Institute of Astronomy and Department of Physics, National Tsing Hua University, Hsinchu 30013, Taiwan
[2] Academia Sinica Institute of Astronomy and Astrophysics, P.O. Box 23-141, Taipei 10617, Taiwan
[3] European Southern Observatory (ESO), Karl-Schwarzschild-Str. 2, D-85748, Garching, Germany
[4] National Astronomical Observatories, Chinese Academy of Sciences, Beijing 100012, People's Republic of China
[5] CAS Key Laboratory of FAST, National Astronomical Observatories, Chinese Academy of Sciences, People's Republic of China
[6] Institut de Ciències de l'Espai (ICE, CSIC), Can Magrans, s/n, E-08193, Cerdanyola del Vallès, Catalonia, Spain
[7] Institut d'Estudis Espacials de Catalunya (IEEC), E-08034, Barcelona, Catalonia, Spain
Received 2019 April 11; revised 2019 September 19; accepted 2019 September 29; published 2020 February 4

Abstract

We report high angular resolution observations of linearly polarized dust emission toward the Class 0 young stellar object NGC1333 IRAS4A (hereafter IRAS4A) using the Karl G. Jansky Very Large Array at *K* (11.5–16.7 mm), *Ka* (8.1–10.3 mm), and *Q* bands (6.3–7.9 mm), and using the Atacama Large Millimeter Array (ALMA) at Band 6 (1.3 mm) and Band 7 (0.85–0.89 mm). On 100–1000 au scales, all of these observations consistently trace the hourglass-shaped magnetic field topology as shown in the previous studies. In the innermost 100 au region of IRAS4A1, the polarization position angles (*E* field) detected at 6.3–16.7 mm are consistent; however, they are nearly 90° offset from those detected at 1.3 mm and 0.85–0.89 mm. Such a 90° offset may be explained by the inner ∼100 au area being optically thick at wavelengths shorter than ∼1.5 mm, whereby the observations probe the absorption of aligned dust against the weakly or unpolarized warm dust emission from the innermost region. This can also consistently explain why the highest angular resolution ALMA images at Band 7 show that the polarization percentage increases with dust brightness temperature in the inner ∼100 au region of IRAS4A1. Following this interpretation and assuming that the dust grains are aligned with the magnetic fields, the inferred magnetic field position angle based on the 90° rotated at 6.3–7.9 mm in the central peak of IRAS4A1 is ∼−22°, which is approximately consistent with the outflow direction of ∼−9°.

Unified Astronomy Thesaurus concepts: Star formation (1569); Magnetic fields (994); Polarimetry (1278); Interstellar medium (847); Protostars (1302)

Supporting material: machine-readable table

1. Introduction

Magnetic fields are believed to play a crucial role in the star formation process (Mouschovias 1977; Shu et al. 1987; Crutcher 2012). Theoretical studies have suggested that magnetic fields can influence the formation of protostellar disks (Li et al. 2014), and can launch outflows and jets from young protostars (Frank et al. 2014). Therefore, detailed measurements of magnetic fields are critical to advancing our understanding of star and disk formation in the early stage.

One of the standard methods of probing the magnetic field structures is to observe the linearly polarized thermal emission from magnetically aligned elongated dust grains. When dust grains are aligned with the magnetic field, the observed polarization position angles of dust thermal emission are expected to be perpendicular to the magnetic field lines. Absorption of continuum background emission by aligned grains can also lead to polarization position angles which are parallel to the magnetic field lines (Hildebrand et al. 2000). Recent studies also show that self scattering of thermal dust emission can also produce the polarization seen at (sub) millimeter or centimeter (Kataoka et al. 2015; Yang et al. 2016). The polarization percentage due to dust scattering is maximized when the largest grain size $a_{\rm max} \sim \lambda/2\pi$, where λ is the observing wavelength (Kataoka et al. 2015). Therefore, multiwavelength dust polarization observations are a necessary tool to determine the mechanism that cause linearly dust polarization.

NGC1333 IRAS4A (hereafter IRAS4A) is one of the best-studied, nearby Class 0 young stellar object (YSO) binary ($d \sim 293$ pc; Ortiz-León et al. 2018; Zucker et al. 2018) in the Perseus Molecular Cloud. It has at least two components, IRAS4A1 and IRAS4A2, separated by 1.″8 (527 au); they both emanate bipolar outflows (Santangelo et al. 2015; Ching et al. 2016). Previous observations of dust polarization (Akeson et al. 1996; Akeson & Carlstrom 1997; Girart et al. 2006; Gonçalves et al. 2008; Frau et al. 2011; Hull et al. 2014; Cox et al. 2015; Liu et al. 2016; Galametz et al. 2018) and CO linear polarization (Girart et al. 1999; Ching et al. 2016) found that on 100–1000 au scales the magnetic field morphology is consistent with an hourglass shape while there may be discrepancies on smaller spatial scales.

To further understand the polarization mechanisms of dust on various sizes scales and wavelengths, we observed NGC1333 IRAS4A using Karl G. Jansky Very Large Array (JVLA) at the *K* (11.5–16.7 mm; 18–26 GHz), *Ka* (8.1–10.3 mm; 29–37 GHz), and *Q* bands (6.3–7.5 mm; 40–48 GHz), and using the Atacama Large Millimeter Array (ALMA) at Band 6 (1.3 mm; 234 GHz) and Band 7 (0.85-0.89 mm; 345 GHz). The details of our multiwavelength observations and data reduction techniques are described in Section 2. The polarization line segments and polarization percentage are presented in

Section 3. Discussion and analysis of our observations are provided in Section 4. The conclusions are given in Section 5.

2. Observations and Data Reduction

2.1. JVLA Observations

We have performed full Stokes polarization observations toward IRAS4A using the JVLA at the *K* and *Ka* bands in the B array configuration, and at the *Q* band in the C and D array configuration. The pointing center for our target source was R.A. = $03^{h}29^{m}10\overset{s}{.}550$ (J2000), decl. = $+31°13'31\overset{''}{.}0$ (J2000). The C array configuration observations at the *Q* band have been introduced in Liu et al. (2016). The D array configuration observations at the *Q* band were carried out on 2015 December 21 (project code 15B-049, PI: Hauyu Baobab Liu). The B array configuration observations at the *K* and *Ka* bands were carried out from mid to late 2016 (project code: 16A-109, PI: Hauyu Baobab Liu). All these observations used the 3 bit sampler, and configured the backend to have an 8 GHz bandwidth coverage by 64 consecutive spectral windows. Other details of these observations are summarized in Table 1.

We manually followed the standard data calibration strategy using the Common Astronomy Software Applications (CASA; McMullin et al. 2007) package, release 5.3.0. After implementing antenna position corrections, weather information, gain-elevation curve and opacity model, we bootstrapped delay fitting and passband calibrations, and then performed complex gain calibration, cross-hand delay fitting, polarization leakage calibration, and polarization position angle referencing. We applied the absolute flux reference to our complex gain solutions, and then applied all derived solution tables to the target source. Finally, we performed three iterations of gain phase self calibrations for the D array configuration observations at the *Q* band to remove the residual phase offsets. Our target source is not bright enough at the *K* band for self-calibrating.

2.2. ALMA Observations

We performed polarization observations toward IRAS4A at Band 6 (1.3 mm, 234 GHz) and Band 7 (0.87 mm, 345 GHz) using ALMA on 2016 November 4 (2016.1.01089.S, PI: Tao-Chung Ching) and on 2016 September 6 (2015.1.00546.S, PI: Shih-Ping Lai), respectively. The ALMA configurations for the 1.3 and 0.87 mm observations are C40-5 with the *uv* distance range from 9 to 865 kλ, and C36-6 with the *uv* distance range from 14 to 2910 kλ, respectively. We utilized the *uv* data calibrated by the ALMA Regional Center (ARC) using the CASA version 4.6.0. Other details of these observations are summarized in Table 1.

2.3. Polarization Images

We imaged the calibrated data using the `tclean` task of the CASA version 5.3.0. We produced images of polarization intensity (PI), polarization percentage (*P*), and polarization position angle (PA) from Stokes *I*, *Q*, *U* maps using the CASA task `immath`. The polarization intensity is debiased using the formula $\mathrm{PI} = \sqrt{Q^2 + U^2 - \sigma_{PI}^2}$, where σ_{PI} is assumed to be the average noise level determined from the Stokes *Q* and *U* maps for simplicity (Simmons & Stewart 1985; Vaillancourt 2006). We evaluated PA as 0.5 arctan (U/Q) and *P* as $(\mathrm{PI}/I) \times 100\%$ from where the *I* and PI intensities were both detected at $>3\sigma$ significance. We follow a convention that PA is defined in between $\pm 90°$; north and east are PA = 0° and 90°, respectively.

3. Results

Figures 1(a) and (c) present polarization line segments taken from all observations overlaid on the 6.9 mm brightness temperature ($T_B^{6.9\mathrm{mm}}$) and the 6.9 to 0.87 mm brightness temperature ratio ($T_B^{6.9\mathrm{mm}}/T_B^{0.87\mathrm{mm}}$), respectively. The images were produced using natural weighting (i.e., Briggs weighting with a robust parameter of 2) to yield the best possible signal-to-noise ratio. To compare the same scales for all the different wavelengths, we used visibilities in the *uv* range of 22–865 kλ and smoothed all images to $0\overset{''}{.}72$ resolution. Our measurements of polarization position angle, percentage, intensity, and Stokes *I*, *Q*, and *U* and their uncertainties at all wavelengths are listed in Table 2 in Appendix A. The polarization maps at the five observed wavelength bands generated using natural weighting and the limited *uv* distance range of 22–865 kλ, are provided in Figure 4 in Appendix B. At projected radii greater than 150 au from IRAS4A1, the polarization position angles at all bands are consistent with each other, and trace the hourglass-shaped magnetic field shown by previous studies (e.g., Girart et al. 2006; Hull et al. 2014). In the central 150 au around IRAS4A1, the polarization position angles detected with JVLA are nearly 90° offset from those detected with ALMA.

A zoom-in of Figure 1(a) toward IRAS4A1 is presented in Figure 1(b). To obtain the detailed distribution at higher angular resolution of polarization line segments around IRAS4A1, we made additional images using the same visibility range but with a robust = −1 for the JVLA *Q* band data and robust = −2 for the ALMA Band 6 data. The resulting images were smoothed to a final $0\overset{''}{.}45$ angular resolution. The 90° offsets are only seen in the innermost 100 au around IRAS4A1. These approximately 90° offsets are also displayed in Figures 2(a) and (b), which show the difference in polarization position angles between ALMA Band 7 and the other bands.

Figure 2(c) shows the polarization percentages in the innermost 100 au region of IRAS4A1, which were measured from images of the five observed wavelength bands generated with $0\overset{''}{.}72$ angular resolution. We caution that the measurements of polarization percentage may be biased by the beam smearing.

Figure 1(d) displays the polarization percentage at ALMA Band 7 overlaid with the polarization line segments using nature weighting. The polarization percentage is generally higher (>10%) in the outer region, dropping to less than 1% toward both IRAS4A1 and IRAS4A2. However, in the innermost 100 au around IRAS4A1, the polarization percentage stops decreasing and climbs back to ∼4%. Figure 2(d) shows the observed polarization percentage versus brightness temperature at 0.87 mm. In addition, in Figures 2(e) and (f) we plot such measurements from the areas which are enclosed by the lowest 6.9 mm Stokes *I* isointensity contours (1.1 mJy beam^{-1}) that isolate IRAS4A1 and IRAS4A2. For IRAS4A1, the polarization percentage decreases at $T_B^{0.87\mathrm{mm}} < 30$ K and increases at $T_B^{0.87\mathrm{mm}} > 30$ K, while for IRAS4A2, the polarization percentage decreases as $T_B^{0.87\mathrm{mm}}$ increases.

Table 1
NGC1333 IRAS4A Observational Parameters

Parameters	JVLA *K* Band		JVLA *Ka* Band		JVLA *Q* Band		ALMA Band 6	ALMA Band 7
Frequency (GHz)	18–26		29–37		40–48		233–235	336–340, 348–352
Wavelength (mm)	11.5–16.7		8.1–10.3		6.3–7.5		1.3	0.85–0.86, 0.88–0.89
Field of view (″)	127		85		62		28	17
Beam size [a] (″), PA (°)	0.36 × 0.32 (−77°)		0.44 × 0.39 (66°)		0.71 × 0.65 (−87°)		0.49 × 0.31 (−7°)	0.25 × 0.18 (−4°)
σ_I [b] (mJy beam^{-1})	0.010		0.040		0.030		2.0	9.0
σ_Q [b] (mJy beam^{-1})	0.0074		0.017		0.014		0.12	0.80
$\sigma_{\rm PI}$ [b] (mJy beam^{-1})	0.0074		0.017		0.014		0.12	0.80
Observing date	2016 Jun 04	2016 Aug 06	2016 Sep 04	2016 Sep 05	2014 Oct 13	2015 Dec 21	2016 Nov 04	2016 Sep 06
Array configuration	B	B	B	B	C	D	C40-5	C36-6
Available antennae	26	27	24	26	26	24	43	39
On-source time (mins)	55	57	51	35	57	56	96	107
Project baseline lengths (meter)	178–10130	216–10650	174–5970	230–8420	36–3140	36–986	12–1110	12–2530
Project baseline lengths ($k\lambda$)	13–922	10–877	169–741	22–1040	5–460	10–877	9–865	14–2910
Gain calibrators	J0336+3218	J0336+3218	J0336+3218	J0336+3218	J0336+3218	J0336+3218	J0336+3218	J0336+3218
Absolute flux calibrators	3C147	3C147	3C147	3C147	3C147	3C147	J0238+1636, J0336+3218	J0238+1636
Bandpass calibrators	3C84	3C84	3C84	3C84	3C84	3C84	J0237+2848, J0238+1636	J0237+2848
Polarization position angle calibrators	3C147	3C147	3C147	3C147	3C147	3C147	J0334-4008	J0334-4008
Leakage calibrators	3C84	3C84	3C84	3C84	3C84	3C84	J0334-4008	J0334-4008
	J2355+4950	J0713+4349	J0713+4349	J0713+4349	J0713+4349	J0713+4349		

Notes.
[a] Measured from the images of limited *uv* distance range of 22–865 $k\lambda$ and nature-weighted.
[b] Measured from the images of limited *uv* distance range of 22–865 $k\lambda$, nature-weighted and smoothed to $0\farcs72$ resolution.

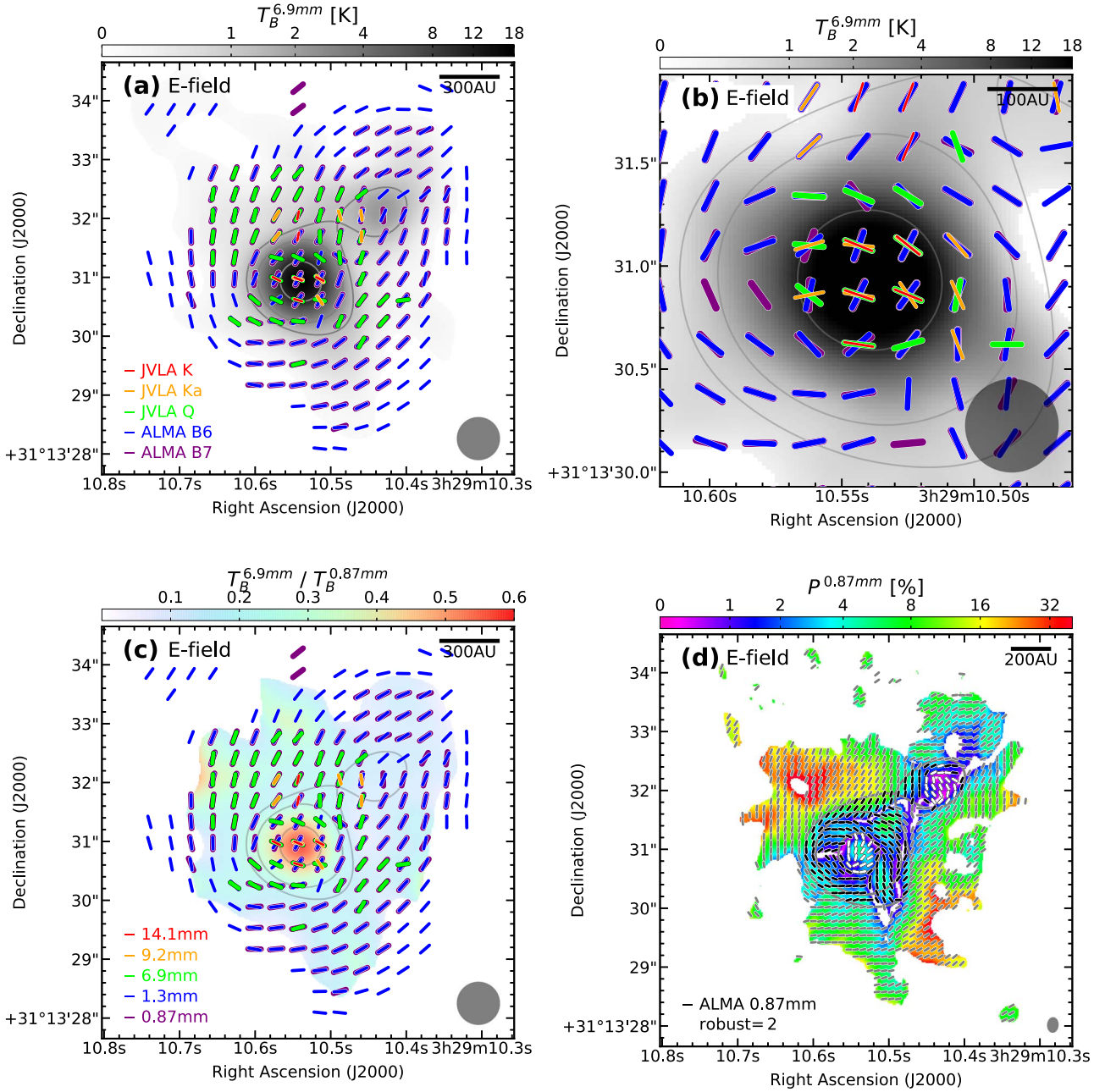

Figure 1. JVLA *K* (14.1 mm), *Ka* (9.2 mm), and *Q* bands (6.9 mm), and ALMA Band 6 (1.3 mm) and Band 7 (0.87 mm) full polarization observations on NGC1333 IRAS4A. (a) The brightness temperature in JVLA 6.9 mm (grayscale) overlaid with the polarization orientations (color line segments) obtained from the smoothed to 0.″72 resolution images. (b) Zoomed image of the panel (a) with the 0.″45 resolution. (c) The brightness temperature ratio of JVLA 6.9 to ALMA 0.87 mm in color scale, and the other parameters are the same as the panel (a). (d) The polarization percentage in ALMA 0.87 mm (color scale) overlaid with the polarization angle (PA) with an angular resolution of $\theta_{\rm maj} \times \theta_{\rm min} = 0.''25 \times 0.''18$ (P.A. $= -3.°6$). The white line segments represent the PA at the innermost 100 au region of IRAS4A1 and IRAS4A2. The black line segments represent the PA at the outside $>35.5 \times \sigma_{\rm I}$ area of the innermost region of IRAS4A1 and IRAS4A2, where $\sigma_{\rm I} = 30$ μJy beam^{-1} for the JVLA 6.9 mm data. The gray line segments represent the PA at the remaining region. The red, orange, green, blue, and purple line segments present the *E*-field polarization position angles observed at both >3 $\sigma_{\rm I}$ and >3 $\sigma_{\rm PI}$ significance for JVLA 14.1 mm, 9.2 mm, and 6.9 mm, and ALMA 1.3 mm and 0.87 mm, respectively. All of the observations are within a limited *uv* distance range of 22–865 $k\lambda$. The levels of gray contours are [1, 2, 4] $\times$ 1.1 mJy beam^{-1} from the 6.9 mm Stokes I intensity map. The synthesized beams are shown in the bottom right of each panel. The scale bars are based on the assumption of a 293 pc distance.

4. Discussion

The observed dust linear polarization can be attributed to aligned dust grains. In the envelope region (∼100–1000 au), the brightness temperature ratio $T_B^{6.9\rm mm}/T_B^{0.87\rm mm}$ is low (∼0.1), which indicates that dust is likely optically thin at all observed wavelengths. Hence, the polarization position angles at all observed wavelengths are parallel to the projected long axis of dust grains. If the dust grains are aligned perpendicular to the magnetic field lines, then the magnetic field morphology inferred from our observations is consistent with a hourglass shape. The polarization observations of CO lines are also trace the consistent magnetic field morphology (Girart et al. 1999; Ching et al. 2016).

In the innermost ∼100 au region around IRAS4A1 (i.e., within the central one beam area of 0.″72 resolution), our observed brightness temperature ratio $T_B^{6.9\rm mm}/T_B^{0.87\rm mm}$ is ∼0.6.

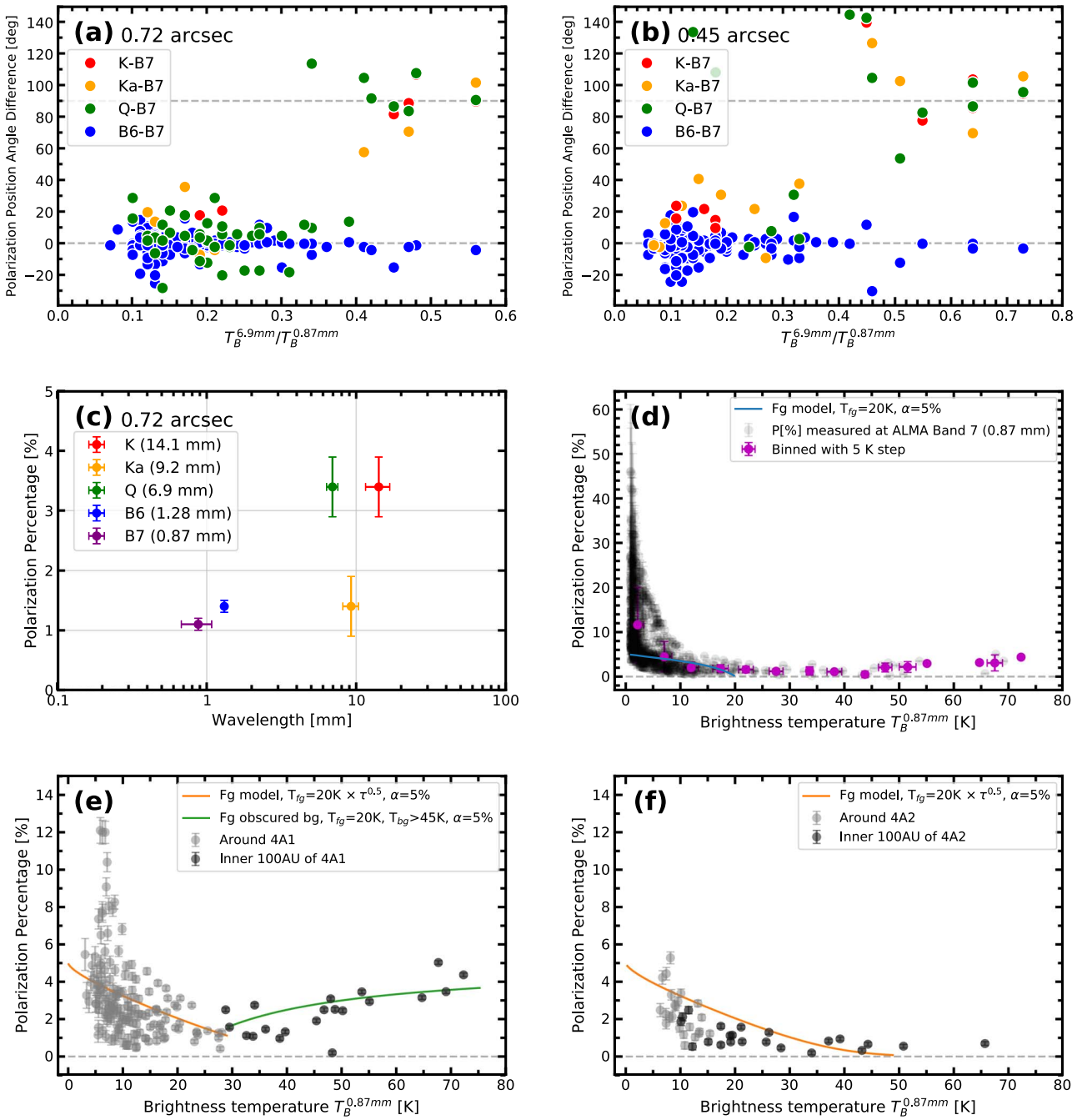

Figure 2. Summary of polarization positional angle difference and polarization percentage. (a) Difference in polarization position angles between ALMA 0.87 mm and JVLA 14.1 mm (*K* band, red dots), 9.2 mm (*Ka* band, orange dots), 6.9 mm (*Q* bands, green dots) and ALMA 1.3 mm (Band 6, blue dots) plotted against the brightness temperature ratio of JVLA 6.9 mm to ALMA 0.87 mm with the $0\farcs72$ resolution. The black dash lines present the angles of 0 and 90°. (b) Similar to panel (a), but using the images generated with the $0\farcs45$ resolution. (c) Polarization percentages in the innermost 100 au region around IRAS4A1 measured from the $0\farcs72$ resolution images. (d) Relation between the polarization percentage and the brightness temperature of ALMA 0.87 mm with an angular resolution of $\theta_{\rm maj} \times \theta_{\rm min} = 0\farcs25 \times 0\farcs18$ (P.A. $= -3\fdg6$). The black points show the original values, and the purple points present the values binned with 5 K step. The blue line represents the model only a foreground envelope with a constant dust temperature $T_{\rm dust} = 20$ K. (e) Relation between the polarization percentage and the brightness temperature of ALMA 0.87 mm around IRAS4A1. The orange line presents the model of one foreground component with $T_{\rm dust} = 20[K] \times \tau^{0.5}$, where τ is from 0 to 2.5. The green line shows the model of a foreground envelope obscured background marginally resolved disk with $T_{\rm dust}^{\rm fg} = 20$ K and $T_{\rm dust}^{\rm bg}$ from 45 to 170 K, respectively. (f) Relation between the polarization percentage and the brightness temperature of ALMA 0.87 mm around IRAS4A2. The orange line presents the model of one foreground component with $T_{\rm dust} = 20[K] \times \tau^{0.5}$, where τ is from 0 to 6. The black and gray points in (e) and (f) represent the polarization percentages of the regions corresponded to the white and black line segments shown in Figure 1(d), respectively.

We derive the optical depth (τ) at 6.9 mm by assuming that the brightness temperature of dust emission is $T_B = T_{\rm dust}(1 - e^{-\tau})$, where the dust temperature ($T_{\rm dust}$) can be factored out. The optical depth at 0.87 mm is approximately $\tau^{0.87{\rm mm}} = \tau^{6.9{\rm mm}} \cdot (6.9\,{\rm mm}/0.87\,{\rm mm})^{\beta}$, where the dust opacity index β is assumed to be 2.0. The corresponding value of $\tau^{6.9{\rm mm}}$ in the innermost ~100 au region of IRAS4A1 is ~0.92, which suggests that the polarization at or longer than 6.9 mm is optically thin or marginally optically thick (Liu et al. 2018). Thus, the polarization observation with JVLA is likely contributed by

polarized dust emission, which is similar to the mechanism at the outside 100 au region of IRAS4A1. On the other hand, the corresponding value of $\tau^{0.87mm}$ is ∼58, which indicates that the dust emission at 0.87 mm and 1.3 mm is already optically thick (Liu et al. 2016; Li et al. 2017; Sahu et al. 2019; Su et al. 2019).

The polarization percentages at all wavelengths in the inner ∼100 au of IRAS4A1 are in the range of 1%–4% and show no obvious relation with wavelength (Figure 2(c)). In addition, based on the analysis of Stokes *I* emission at (sub)millimeter and centimeter wavelength bands, Li et al. (2017) found that the dust opacity spectral index is consistent with ∼2, which is not distinguishable from that in the diffuse interstellar medium (for a more recent discussion, see Galván-Madrid et al. 2018). Conventionally, the ∼2 values of dust opacity spectral index would infer that the maximum grain sizes are less than 100 μm (see Testi et al. 2014 and references therein). The inferred values of maximum grain sizes may be still smaller after the effects of dust scattering opacity is self consistently considered (Liu 2019; Zhu et al. 2019, and Tazaki et al. 2019). If it is indeed the case, then the polarization due to dust self scattering should be nondetectable at wavelengths longer than 6.9 mm (see Figure 3 of Kataoka et al. 2016). Recent studies of the Class II YSOs also suggests that the maximum grain size should be $\lesssim$100 μm (e.g., Kataoka et al. 2017; Stephens et al. 2017; Hull et al. 2018; Ohashi et al. 2018; Dent et al. 2019; Okuzumi & Tazaki 2019), inferring that the maximum polarization generated by the self scattering is $\lesssim$1% (Kataoka et al. 2015). Given that dust grains in Class 0 YSOs are likely smaller than those in Class II YSOs, we argue that on the spatial scale and wavelength range probed by our polarization observations, dust self scattering may not be a significant polarization mechanism. As to the radiative alignment, we cannot rule out this possibility without spatially resolving the innermost ∼100 au region of IRAS4A1. Nevertheless, we disfavor the radiative alignment due to that it predicts no polarization at the central location.

We hypothesize that in this case the JVLA observations are indicative of polarized emission from aligned dust grains, while the ALMA observations point toward extinction due to aligned dust grain. This can help explain the 90° offset of the polarization position angles observed by these two instruments. This explanation is supported by the radiative transfer simulation with POLARIS (Reissl et al. 2017). Following this interpretation, we hypothesize that at wavelengths longer than 6.9 mm, the 90°-relationed polarization position angles trace the projected B-field orientation (Figure 3). The inferred B-field position angles in the central 100 au around IRAS4A1 is ∼−22°, which is approximately consistent with the outflow position angles of ∼−9° (Ching et al. 2016).

In Figures 2(d)–(f), we provide a simplified model to qualitatively explain the observed polarization percentage distribution at 345 GHz. Our fiducial simplified model is composed of two components: one foreground component, which can be illustrated as the circumstellar envelope on ∼100–1000 au scales; and one (foreground) obscured background component, which can be illustrated as a marginally resolved disk on $\lesssim$100 au scales, obscured by the foreground circumstellar envelope.

Assuming that dust on 100–1000 au scales is predominantly heated by the stellar irradiation from IRAS4A1, and assuming an approximate thermal equilibrium, the dust temperature $T_{\rm dust}$ should have an $r^{-\frac{1}{2}}$ dependence according to the Stefan-Boltzmann law, where r is the radius from the host protostar of IRAS4A1.

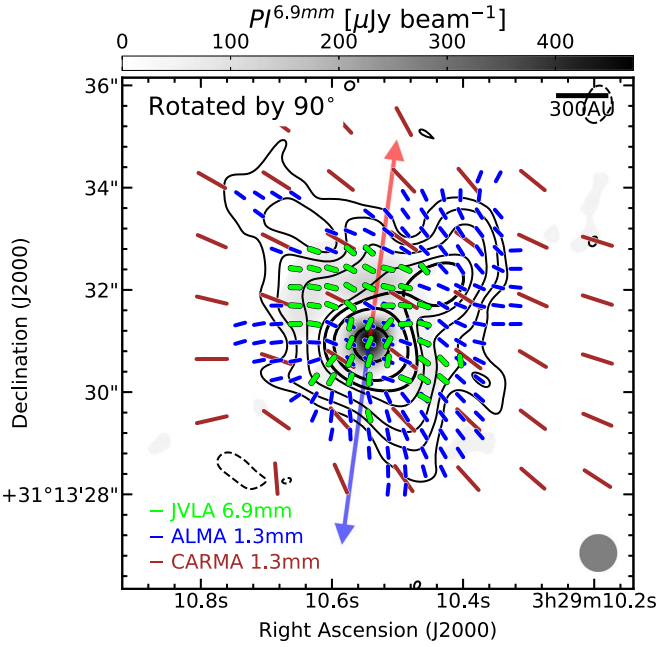

Figure 3. Comparison of position angles (after 90° rotated from the *E*-field orientation) at 6.9 mm by JVLA (green), at 1.3 mm by ALMA (blue), and 1.3 mm by CARMA (brown, Hull et al. 2014). The JVLA and ALMA images presented in this panel were generated using a limited *uv* distance range of 22–865 $k\lambda$ and were smoothed to the 0.″72 resolution. Polarization intensity at 6.9 mm is presented in grayscale. Contours present the 6.9 mm Stokes I continuum emission. Contour levels are 30 μJy beam (1σ) × [−3, 3, 6, 12, 24, 35.5, 71, 284]. The red and blue arrows represent the axis of −9° in the IRAS4A1 redshifted and the blueshifted outflows (Ching et al. 2016), respectively.

Assuming that the mass volume density around IRAS4A1 can be approximated by a singular isothermal sphere (Shu 1977), then the volume density n has a r^{-2} dependence. The dust column density $\Sigma_{\rm dust}$ and optical depth τ then have r^{-1} dependence. Therefore, in the envelope we approximately have $T_{\rm dust} \propto \tau^{0.5}$.

Based on the spectral energy distribution (SED) fittings, Li et al. (2017) suggested that the envelope component has a dust temperature $T_{\rm dust} \sim 20$ K and the dust optical depths ∼1 in the inner ∼100 au region. Motivated by these measurements, we adopted the $T_{\rm dust}$ values and the dust optical depth at the two orthogonal linear polarization orientation (*E* and *B*), τ^E and τ^B, following

$$T_{\rm dust} = 20[K] \times \tau^{\frac{1}{2}},\ \tau^B \equiv (1-\alpha)\tau,\ \tau^E \equiv (1+\alpha)\tau, \quad (1)$$

where α is the polarization efficiency. We assume α to be a 5% constant. We evaluated the brightness temperatures T^B and T^E on the area where the fore/background components are not overlapped by

$$T^B = \frac{1}{2}T_{\rm dust}(1-e^{-\tau^B}),\ T^E = \frac{1}{2}T_{\rm dust}(1-e^{-\tau^E}), \quad (2)$$

The Stokes I intensity (*I*), polarized intensity (PI), and polarization percentage (*P*) are $T^B + T^E$, $T^B - T^E$, and $|PI/I|$, respectively. By varying τ, the obtained *P* as a function of *I* is shown as the orange curve in Figures 2(e) and (f) to compare with the observations around IRAS4A1 and IRAS4A2, respectively. For IRAS4A2, the observed polarization percentage is below the predicted model as shown in Figure 2(f). This may partly due to a forest of spectral lines

(Sahu et al. 2019), which leads to an overestimate of Stokes *I* continuum flux and consequently an underestimate of polarization percentage. For comparison, we have also done the similar evaluation, but assuming a constant $T_{\rm dust} = 20$ K, which is shown as the blue curve in Figure 2(d).

We assumed that the background component (e.g., the disk) has a >45 K dust temperature ($T_{\rm dust}^{\rm bg}$) distribution, which was also motivated by the SED fittings of Li et al. (2017). We further assumed that in the area that the foreground component (e.g., the envelope) is obscuring the background component, the foreground component has an average dust temperature ~20 K and the average optical depth $\tau \sim 1$. We evaluated T^B and T^E by

$$T^B = \frac{1}{2} T_{\rm dust}^{\rm bg} e^{-\tau^B} + \frac{1}{2} T_{\rm dust}(1 - e^{-\tau^B}), \quad (3)$$

$$T^E = \frac{1}{2} T_{\rm dust}^{\rm bg} e^{-\tau^E} + \frac{1}{2} T_{\rm dust}(1 - e^{-\tau^E}), \quad (4)$$

and then *I*, PI, and *P* was evaluated by varying the values of $T_{\rm dust}^{\rm bg}$ and fixing the other parameters (see Liu et al. 2018). The resulting fitted *P* as a function of *I* is shown as the green curve in Figure 2(e), which covers the innermost ~100 au region of IRAS4A1.

This simple two-component model can qualitatively explain the observed trends of *P* at 345 GHz. We did not intend to perform detailed fitting due to the uncertainty in the assumption of α, the uncertainties of *P* due to polarization canceling in a finite synthesized beam, and the missing fluxes over extended angular scales which can bias high the observed *P* at regions with low *I*. Furthermore, our target source is in fact a binary which likely has a more complicated density and temperature structure than what can be reproduced by assuming very few free parameters.

5. Conclusions

We have performed full polarization observations with JVLA at 11.5–16.7, 8.1–10.3 and 6.3–7.5 mm, and with ALMA at 1.3 and 0.85–0.89 mm toward the Class 0 YSO NGC1333 IRAS4A. We have successfully detected linear polarization from all observations. Our JVLA *K*-band data offer the dust polarization ever detected at longest wavelengths in YSOs. We found that the polarization angles from all bands are consistent with each other on the larger 100–1000 au scales from IRAS4A1, while on the innermost ~100 au scales around IRAS4A1 the polarization angles of JVLA data and ALMA data are approximately perpendicular to each other. This 90° offset can be explained if the polarization originates from aligned dust grains at different optical depths; the dust emission is marginally optically thick or optically thin at JVLA bands and is optically thick at ALMA Bands. Thus, the polarization at ALMA bands suffers from foreground extinction which leads to the observed polarization being perpendicular to the magnetic field. In addition, the variation of polarization can also be modeled with polarization of aligned dust grains from an optically thick background source with a foreground envelope. The magnetic field direction around IRAS4A1 inferred from the aligned dust grains is ~−22°, which is very close to the outflow position angles of ~−9°, suggesting that magnetic fields are important for launching outflows.

We thank the anonymous referee for the helpful comments. This paper makes use of the following ALMA data: ADS/JAO.ALMA #2015.1.00546.S, #2016.1.01089.S. ALMA is a partnership of ESO (representing its member states), NSF (USA) and NINS (Japan), together with NRC (Canada), MOST and ASIAA (Taiwan), and KASI (Republic of Korea), in cooperation with the Republic of Chile. The Joint ALMA Observatory is operated by ESO, AUI/NRAO, and NAOJ. H. B.L. and C.L.K. are supported by the Ministry of Science and Technology (MoST) of Taiwan (grant No. 108-2112-M-001-002-MY3). C.L.K. and S.P.L. acknowledge support from the Ministry of Science and Technology of Taiwan with grant MOST 106-2119-M-007-021-MY3. J.M.G. is supported by Spanish MINECO AYA2017-84390-C2-1-R grant..

Facilities: ALMA, VLA.

Software: CASA (v5.3.0 + 4.6.0, McMullin et al. 2007), Numpy (van der Walt et al. 2011), APLpy (Robitaille & Bressert 2012).

Appendix A
Polarization Measurements

Table 2 shows the Stokes *I*, *Q*, *U* intensities, polarization intensity (PI), polarization position angle (PA), polarization percentage (*P*) and their uncertainties taken at the positions of the polarization segments present in Figures 1(a) and (d). Details of the observations, data reduction, and imaging are outlined in Section 2.

Table 2
Polarization Measurements from All the Observations[a]

# [a]	R.A. (J2000) (deg)	Decl. (J2000) (deg)	Stokes I (Jy beam^{-1})	Stokes *Q* (Jy beam^{-1})	Stokes U (Jy beam^{-1})	PI (Jy beam^{-1})	PA (deg)	δPA[b] (deg)	P (%)	δP[c] (%)
JVLA *K* band (11.5–16.7 mm; 18–26 GHz; beam size: 0.″72 × 0.″72; $\sigma_{\rm I}$ ~ 1e-5 Jy beam^{-1}; $\sigma_Q \sim \sigma_{\rm U} \sim \sigma_{\rm PI}$ ~ 7.4e-6 Jy beam^{-1})										
1	52.29393	31.22517	1.05e-03	−2.96e-05	2.01e-05	3.50e-05	73	0.1	3.3	0.7
1	52.29405	31.22527	6.94e-04	−1.73e-05	2.39e-05	2.86e-05	63	0.13	4.1	1.1
1	52.29393	31.22527	1.57e-03	−3.66e-05	4.06e-05	5.42e-05	66	0.068	3.4	0.5
1	52.29381	31.22527	1.14e-03	−1.86e-05	2.31e-05	2.87e-05	64	0.12	2.5	0.65
1	52.29393	31.22547	1.87e-04	2.95e-05	−1.27e-05	3.12e-05	−12	0.12	17	4.1
1	52.29393	31.22557	6.51e-05	3.50e-05	−1.52e-05	3.75e-05	−12	0.097	58	15
JVLA *Ka* band (8.1–10 mm; 29-37 GHz; beam size: 0.″72 × 0.″72; $\sigma_{\rm I}$ ~ 4e-5 Jy beam^{-1}; $\sigma_Q \sim \sigma_{\rm U} \sim \sigma_{\rm PI}$ ~1.7e-5 Jy beam^{-1})										
2	52.29381	31.22517	2.81e-03	2.56e-05	6.32e-05	6.60e-05	34	0.12	2.4	0.61
2	52.29393	31.22527	5.55e-03	−7.31e-05	3.20e-05	7.79e-05	78	0.11	1.4	0.5

Table 2
(Continued)

# [a]	R.A. (J2000) (deg)	Decl. (J2000) (deg)	Stokes I (Jy beam^{-1})	Stokes Q (Jy beam^{-1})	Stokes U (Jy beam^{-1})	PI (Jy beam^{-1})	PA (deg)	δPA [b] (deg)	P (%)	δP [c] (%)
2	52.29381	31.22527	4.01e-03	−1.54e-06	7.52e-05	7.33e-05	46	0.11	1.8	0.5
2	52.29405	31.22547	4.93e-04	1.20e-05	−5.56e-05	5.42e-05	−39	0.15	11	3.6
2	52.29358	31.22547	4.23e-04	5.39e-05	−8.79e-07	5.12e-05	−0	0.16	12	4.2
...										
JVLA Q band (6.3–7.5 mm; 40-48 GHz; beam size: 0.″72 × 0.″72; $\sigma_I \sim$ 3e-5 Jy beam^{-1}; $\sigma_Q \sim \sigma_U \sim \sigma_{PI} \sim$ 1.4e-5 Jy beam^{-1})										
3	52.29393	31.22487	2.69e-04	−4.73e-05	−2.97e-05	5.41e-05	−74	0.13	20	5.7
3	52.29358	31.22497	5.27e-04	3.07e-05	−5.19e-05	5.87e-05	−30	0.12	11	2.7
3	52.29428	31.22507	3.63e-04	−1.71e-05	4.52e-05	4.62e-05	55	0.14	13	4
3	52.29417	31.22507	6.17e-04	−2.96e-05	5.16e-05	5.78e-05	60	0.12	9.4	2.3
3	52.29405	31.22507	1.30e-03	−4.22e-05	3.96e-05	5.61e-05	68	0.12	4.3	1.1
...										
ALMA Band 6 (1.3 mm; 234 GHz; beam size: 0.″72 × 0.″72; $\sigma_I \sim$ 2e-3 Jy beam^{-1}; $\sigma_Q \sim \sigma_U \sim \sigma_{PI} \sim$ 1.2e-4 Jy beam^{-1})										
4	52.29381	31.22447	6.75e-03	−1.15e-03	2.36e-04	1.17e-03	84	0.051	17	5.5
4	52.29370	31.22447	7.27e-03	−1.09e-03	2.13e-04	1.10e-03	84	0.054	15	4.5
4	52.29381	31.22457	1.05e-02	−1.50e-03	−4.47e-05	1.50e-03	−89	0.04	14	3
4	52.29370	31.22457	1.14e-02	−1.29e-03	−1.64e-04	1.30e-03	−86	0.046	11	2.3
4	52.29358	31.22457	8.89e-03	−1.01e-03	−6.21e-04	1.18e-03	−74	0.051	13	3.3
...										
ALMA Band 7 (0.87 mm; 345 GHz; beam size: 0.″72 × 0.″72; $\sigma_I \sim$ 9e-3 Jy beam^{-1}; $\sigma_Q \sim \sigma_U \sim \sigma_{PI} \sim$ 8e-4 Jy beam^{-1})										
5	52.29370	31.22457	3.20e-02	−3.70e-03	−2.54e-03	4.42e-03	−73	0.089	14	4.7
5	52.29381	31.22467	4.80e-02	−4.53e-03	−2.18e-03	4.96e-03	−77	0.08	10	2.6
5	52.29370	31.22467	4.76e-02	−4.35e-03	−3.31e-03	5.41e-03	−71	0.073	11	2.7
5	52.29358	31.22467	2.94e-02	−4.90e-03	−5.52e-03	7.34e-03	−66	0.054	25	8.2
5	52.29417	31.22477	2.88e-02	−3.48e-03	6.53e-05	3.39e-03	89	0.11	12	4.7
...										
ALMA Band 7 (0.87 mm; 345 GHz; beam size: 0.″25 × 0.″18; $\sigma_I \sim$ 1.2e-3 Jy beam^{-1}; $\sigma_Q \sim \sigma_U \sim \sigma_{PI} \sim$ 9e-5 Jy beam^{-1})										
6	52.293113	31.224472	0.0037	−0.0002	−0.00027	0.00033	−63	0.13	8.8	3.8
6	52.293074	31.224472	0.0041	−0.0002	−0.00022	0.00029	−66	0.15	6.9	3
6	52.293113	31.224505	0.005	−0.00017	−0.00032	0.00035	−59	0.12	7.1	2.5
6	52.293074	31.224505	0.0055	−0.0002	−0.00031	0.00035	−61	0.12	6.4	2.2
6	52.293074	31.224539	0.0039	−0.0002	−0.00034	0.00039	−60	0.11	10	3.9
...										

Notes. All of the measurements are from the images of limited uv distance range of 22–865 kλ and naturally weighted.
[a] Each number represents the following observation: (1) JVLA K band (beam size: 0.″72 × 0.″72), (2) JVLA Ka band (beam size: 0.″72 × 0.″72), (3) JVLA Q band (beam size: 0.″72 × 0.″72), (4) ALMA Band 6 (beam size: 0.″72 × 0.″72), (5) ALMA Band 7 (beam size: 0.″72 × 0 .″72), (6) ALMA Band 7 (beam size: 0.″25 × 0.″18)
[b] The uncertainty of polarization position angle does not take into account the systematic calibration uncertainty.
[c] We have considered the systematic calibration uncertainties in polarization percentages, which is 0.5% and 0.1% for the JVLA and the ALMA observations, respectively, according to the Guide to Observing with the VLA (https://science.nrao.edu/facilities/vla/docs/manuals/obsguide/modes/pol) and the ALMA Cycle 3 and Cycle 4 Technical Handbook (https://almascience.nrao.edu/documents-and-tools/cycle4/alma-technical-handbook/view).

(This table is available in its entirety in machine-readable form.)

Appendix B
Polarization Images

Figure 4 shows the Stokes I intensity, polarization intensity (PI), and polarization position angle (PA) images with JVLA at 11.5–16.7, 8.1–10.3 and 6.3–7.5 mm, and with ALMA at 1.3 and 0.85–0.89 mm toward the Class 0 YSO NGC1333 IRAS4A. The images were generated using natural weighting and the limited uv distance range of 22–865 $k\lambda$ with the angular resolution listed in Table 1.

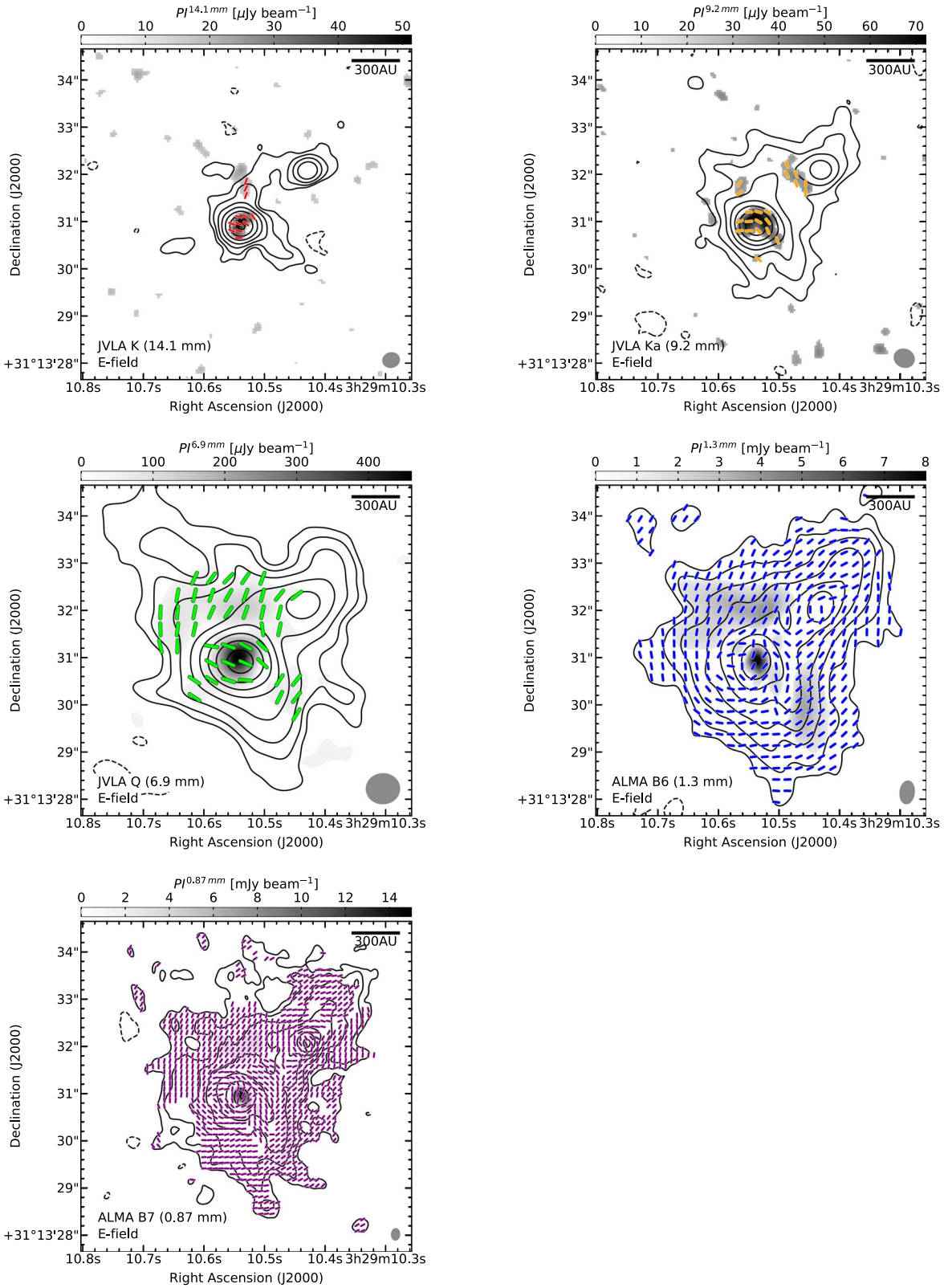

Figure 4. JVLA *K* (14.1 mm), *Ka* (9.2 mm), and *Q* bands (6.9 mm), and ALMA Band 6 (1.3 mm) and Band 7 (0.87 mm) full polarization observations on NGC1333 IRAS4A. The polarization intensities are presented in grayscale. Contours present the Stokes *I* intensities. The line segments present the *E*-field polarization position angles observed at both $>3\,\sigma_{\rm I}$ and $>3\sigma_{\rm PI}$ significance for each band with the angular resolution listed in Table 1. The levels of contours are [−1, 1, 2, 4, 8, 16, 32, 64, and 128] × 3 $\sigma_{\rm I}$, where $\sigma_{\rm I}$ = 5.2, 14, 26, 750, and 1200 μJy beam^{-1} for the JVLA *K*, *Ka*, *Q* band, and ALMA Band 6, and Band 7 Stokes *I* images, respectively. All the observations are within a limited *uv* distance range of 22–865 $k\lambda$.

ORCID iDs

Chia-Lin Ko (柯嘉琳) https://orcid.org/0000-0003-2158-8141
Hauyu Baobab Liu (呂浩宇) https://orcid.org/0000-0003-2300-2626
Shih-Ping Lai (賴詩萍) https://orcid.org/0000-0001-5522-486X
Tao-Chung Ching (慶道沖) https://orcid.org/0000-0001-8516-2532
Ramprasad Rao https://orcid.org/0000-0002-1407-7944
Josep Miquel Girart https://orcid.org/0000-0002-3829-5591

References

Akeson, R. L., & Carlstrom, J. E. 1997, ApJ, 491, 254
Akeson, R. L., Carlstrom, J. E., Phillips, J. A., & Woody, D. P. 1996, ApJL, 456, L45
Ching, T.-C., Lai, S.-P., Zhang, Q., et al. 2016, ApJ, 819, 159
Cox, E. G., Harris, R. J., Looney, L. W., et al. 2015, ApJL, 814, L28
Crutcher, R. M. 2012, ARA&A, 50, 29
Dent, W. R. F., Pinte, C., Cortes, P. C., et al. 2019, MNRAS, 482, L29
Frank, A., Ray, T. P., Cabrit, S., et al. 2014, in Protostars and Planets VI, ed. H. Beuther et al. (Tucson, AZ: Univ. Arizona Press), 451
Frau, P., Galli, D., & Girart, J. M. 2011, A&A, 535, A44
Galametz, M., Maury, A., Girart, J. M., et al. 2018, A&A, 616, A139
Galván-Madrid, R., Liu, H. B., Izquierdo, A. F., et al. 2018, ApJ, 868, 39
Girart, J. M., Crutcher, R. M., & Rao, R. 1999, ApJL, 525, L109
Girart, J. M., Rao, R., & Marrone, D. P. 2006, Sci, 313, 812
Gonçalves, J., Galli, D., & Girart, J. M. 2008, A&A, 490, L39
Hildebrand, R. H., Davidson, J. A., Dotson, J. L., et al. 2000, PASP, 112, 1215
Hull, C. L. H., Plambeck, R. L., Kwon, W., et al. 2014, ApJS, 213, 13
Hull, C. L. H., Yang, H., Li, Z.-Y., et al. 2018, ApJ, 860, 82
Kataoka, A., Muto, T., Momose, M., et al. 2015, ApJ, 809, 78
Kataoka, A., Muto, T., Momose, M., Tsukagoshi, T., & Dullemond, C. P. 2016, ApJ, 820, 54
Kataoka, A., Tsukagoshi, T., Pohl, A., et al. 2017, ApJL, 844, L5
Li, J. I.-H., Liu, H. B., Hasegawa, Y., & Hirano, N. 2017, ApJ, 840, 72
Li, Z.-Y., Krasnopolsky, R., Shang, H., & Zhao, B. 2014, ApJ, 793, 130
Liu, H. B. 2019, ApJL, 877, L22
Liu, H. B., Hasegawa, Y., Ching, T.-C., et al. 2018, A&A, 617, A3
Liu, H. B., Lai, S.-P., Hasegawa, Y., et al. 2016, ApJ, 821, 41
McMullin, J. P., Waters, B., Schiebel, D., Young, W., & Golap, K. 2007, in ASP Conf. Ser. 376, Astronomical Data Analysis Software and Systems XVI, ed. R. A. Shaw, F. Hill, & D. J. Bell (San Francisco, CA: ASP), 127
Mouschovias, T. C. 1977, ApJ, 211, 147
Ohashi, S., Kataoka, A., Nagai, H., et al. 2018, ApJ, 864, 81
Okuzumi, S., & Tazaki, R. 2019, ApJ, 878, 132
Ortiz-León, G. N., Loinard, L., Dzib, S. A., et al. 2018, ApJ, 865, 73
Reissl, S., Seifried, D., Wolf, S., et al. 2017, A&A, 603, A71
Robitaille, T., & Bressert, E. 2012, APLpy: Astronomical Plotting Library in Python, Astrophysics Source Code Library, ascl:1208.017
Sahu, D., Liu, S.-Y., Su, Y.-N., et al. 2019, ApJ, 872, 196
Santangelo, G., Codella, C., Cabrit, S., et al. 2015, A&A, 584, A126
Shu, F. H. 1977, ApJ, 214, 488
Shu, F. H., Adams, F. C., & Lizano, S. 1987, ARA&A, 25, 23
Simmons, J. F. L., & Stewart, B. G. 1985, A&A, 142, 100
Stephens, I. W., Yang, H., Li, Z.-Y., et al. 2017, ApJ, 851, 55
Su, Y.-N., Liu, S.Y., Li, Z.-Y., et al. 2019, ApJ, 885, 98
Tazaki, R., Tanaka, H., Kataoka, A., Okuzumi, S., & Muto, T. 2019, ApJ, 885, 52
Testi, L., Birnstiel, T., Ricci, L., et al. 2014, in Protostars and Planets VI, ed. H. Beuther et al. (Tucson, AZ: Univ. Arizona Press), 339
Vaillancourt, J. E. 2006, PASP, 118, 1340
van der Walt, S., Colbert, S. C., & Varoquaux, G. 2011, CSE, 13, 22
Yang, H., Li, Z.-Y., Looney, L. W., et al. 2016, MNRAS, 460, 4109
Zhu, Z., Zhang, S., Jiang, Y.-F., et al. 2019, ApJL, 877, L18
Zucker, C., Schlafly, E. F., Speagle, J. S., et al. 2018, ApJ, 869, 83